





Article

Fe-Doping in Double Perovskite $\text{PrBaCo}_{2(1-x)}\text{Fe}_{2x}\text{O}_{6-\delta}$: Insights into Structural and Electronic Effects to Enhance Oxygen Evolution Catalyst Stability

Bae-Jung Kim ^{1,*} , Emiliana Fabbri ^{1,*} , Ivano E. Castelli ² , Mario Borlaf ³ , Thomas Graule ³, Maarten Nachtegaal ¹ and Thomas J. Schmidt ^{1,4}

¹ Paul Scherrer Institut, Forschungstrasse 111, 5232 Villigen PSI, Switzerland; maarten.nachtegaal@psi.ch (M.N.); thomasjustus.schmidt@psi.ch (T.J.S.)

² Department of Energy Conversion and Storage, Fysikvej 309, Technical University of Denmark, DK-2800 Kgs. Lyngby, Denmark; ivca@dtu.dk

³ Laboratory for High Performance Ceramics, Empa, Swiss Federal Laboratories for Materials Testing and Research, 8600 Dübendorf, Switzerland; mario.borlaf@empa.ch (M.B.); thomas.graule@empa.ch (T.G.)

⁴ Laboratory of Physical Chemistry, ETH Zürich, CH-8093 Zürich, Switzerland

* Correspondence: joseph.kim@psi.ch (B.-J.K.); emiliana.fabbri@psi.ch (E.F.); Tel.: +41-56-310-4580 (B.K.); +41-56-310-2795 (E.F.)

Received: 19 February 2019; Accepted: 12 March 2019; Published: 14 March 2019



Abstract: Perovskite oxides have been gaining attention for its capability to be designed as an ideal electrocatalyst for oxygen evolution reaction (OER). Among promising candidates, the layered double perovskite— $\text{PrBaCo}_2\text{O}_{6-\delta}$ (PBC)—has been identified as the most active perovskite electrocatalyst for OER in alkaline media. For a single transition metal oxide catalyst, the addition of Fe enhances its electrocatalytic performance towards OER. To understand the role of Fe, herein, Fe is incorporated in PBC in different ratios, which yielded $\text{PrBaCo}_{2(1-x)}\text{Fe}_{2x}\text{O}_{6-\delta}$ ($x = 0, 0.2$ and 0.5). Fe-doped PBCF's demonstrate enhanced OER activities and stabilities. Operando X-ray absorption spectroscopy (XAS) revealed that Co is more stable in a lower oxidation state upon Fe incorporation by establishing charge stability. Hence, the degradation of Co is inhibited such that the perovskite structure is prolonged under the OER conditions, which allows it to serve as a platform for the oxy(hydroxide) layer formation. Overall, our findings underline synergetic effects of incorporating Fe into Co-based layered double perovskite in achieving a higher activity and stability during oxygen evolution reaction.

Keywords: Fe-substitution; operando X-ray absorption spectroscopy; oxygen evolution reaction; double perovskite catalysts; oxy(hydroxide)

1. Introduction

Today, modern society is evolving to become more energy dependent. As the awareness of environmental impact from current energy systems is elevating, more efforts recently have been devoted towards mainstreaming renewable energy sources. However, the implementation of renewable energy technologies is challenging, as it requires an efficient energy storage system to mediate the intermittent generation and consumption of energy. The electrochemical splitting of water (i.e., water electrolysis) offers an effective method to produce large amounts of hydrogen (H_2), which can be stored and used as an energy vector [1]. Therefore, an efficient oxygen evolution reaction (OER) is essential since it is the key reaction in water electrolysis. During the past decade, the members of the perovskite oxide family (ABO_3) have been gaining vast attention for their promising activities as OER electrocatalysts under alkaline conditions, and thereby relieving the need of expensive precious metals such as iridium [2–7]. Generally, perovskite oxides are composed of rare-earth (e.g., lanthanides) or

earth alkaline metals (e.g., Ba) in the A-site and 3D transition metals in the B-site (e.g., Ni, Co and/or Fe). The perovskites intrinsic properties can be tailored through partial cation substitution [2,8,9]. This substitution can transpire in both A- and B-sites of the perovskite (i.e., $A'_{1-n}A''_nB'_{1-m}B''_mO_3$; $0 \leq n, m \leq 1$) either in ordered or random arrangement [10]. Likewise, cation ordering plays an important role in engineering the intrinsic properties of a perovskite such as electronic structure, ionic conductivity, and magnetic properties, all of which may change its electrocatalytic behavior [3,10,11]. The recently proposed OER mechanism emphasizes that the formation of oxy(hydroxide) layer at metal oxide surface is essential along the path of lattice oxygen evolution reaction (LOER) [12,13]. In this context, developing perovskite oxides as OER catalyst is advantageous, owing to its ability to exhibit high oxygen vacancy concentration upon cation substitution and ordering it so as to activate the LOER [14,15]. In contrast to the conventional OER mechanism [16,17], in the case where the lattice oxygen is directly involved (i.e., LOER), the high surface OH^- coverage from the alkaline media is no longer necessary as loosely bonded lattice oxygen atoms act as the reaction intermediates itself; as a result, the overpotential is lowered [12,18]. In this regard, the use of layered double perovskite oxides ($A'_{2(1-n)}A''_{2n}B'_{2(1-m)}B''_{2m}O_6$; $0 \leq n, m \leq 1$) is beneficial as they tend to localize the oxygen vacancies into layers through A-site ordering and promote high oxygen mobility [14]. Among the layered double perovskite family, $PrBaCo_2O_{6-\delta}$ (PBC) has been appraised for its high OER activity [19–24]. Nevertheless, past studies point out the instability of PBC under OER conditions [2,13,23,25–27], raising queries regarding its degradation mechanism. In our recent study [2], we highlighted that the degradation is a kinetic process and every catalyst varies in how it reaches the end of its service life depending on the inherent properties.

In a different perspective, a single randomly ordered perovskite oxide, $Ba_{0.5}Sr_{0.5}Co_{0.8}Fe_{0.2}O_{3-\delta}$ (BSCF), has been identified as another highly active OER catalyst [5,22,27,28]. More recently, we have reported that highly oxygen deficient BSCF prepared via flame spray synthesis would lead to the participation of lattice oxygen atoms (i.e., LOER) coupled with the OER process. Based on operando X-ray absorption spectroscopy (XAS) results [2,24,27] and density-functional theory (DFT) based calculations [2,24], BSCF is capable of facilitating the formation of a self-constructed oxy(hydroxide) surface layer during OER, owing to its thermodynamic nature of meta-stability under the OER condition. Intriguingly, in the means to understand each individual chemical component of BSCF, recent findings highlight the vital role of Fe in its B-site so as to pertain to the thermodynamic meta-stability, and provide charge stability [24]. Likewise, many studies have reported constructive effect of incorporating Fe into 3D transition metal oxide catalysts for OER [29–38].

Therefore, in this study, we incorporate Fe into the B-site of PBC in different ratios to yield $PrBaCo_{2(1-x)}Fe_{2x}Co_{6-\delta}$ ($x = 0.2$ and 0.5 ; denoted as PBCF82 and PBCF55, respectively) for the purpose of tailoring the electrocatalytic performance with respect to OER activity and stability. Nanoparticles of all the materials under study are attained via flame spray synthesis [39]. Operando XAS is used to gain insights into changes in local electronic and geometric structures of the layered double perovskites upon Fe-doping. Combined with the thermodynamic nature inferred from DFT calculations, the roles of Fe in the layered double perovskite as OER catalyst are highlighted. Based on our findings, we underline the synergetic effect that Fe conveys and elucidate the enhanced OER performance of layered double perovskite catalyst upon Fe incorporation.

2. Results and Discussion

2.1. Physical Characterization

All perovskite catalysts— $PrBaCo_{2(1-x)}Fe_{2x}Co_{6-\delta}$ ($x = 0, 0.2$, and 0.5 ; denoted as PBC, PBCF82, and PBCF55, respectively)—are prepared via flame spray synthesis from which nano-scaled particles are obtained (Figure 1). Metal precursors are dissolved in combustible solution and injected into the flame at high temperature (possible up to $\approx 3000^\circ C$) and the resulting precipitates are collected. Previously, we have established the benefits of this particular synthesis of perovskites for the electrocatalytic

performance [2,27]. The physical and structural traits of such nanoparticles are observed using transmission electron microscopy (TEM) (Figure 1). Figure 1a–c show the TEM images of the prepared nanoparticles of PBC, PBCF82, and PBCF55, respectively. All of the prepared nanoparticles are in sizes that range from 5–30 nm. Each inset of Figure 1a–c shows high-resolution (HR) TEM images of PBC, PBCF82, and PBCF55, respectively, and each reveals clear fringes, indicating the formation of crystalline structures.

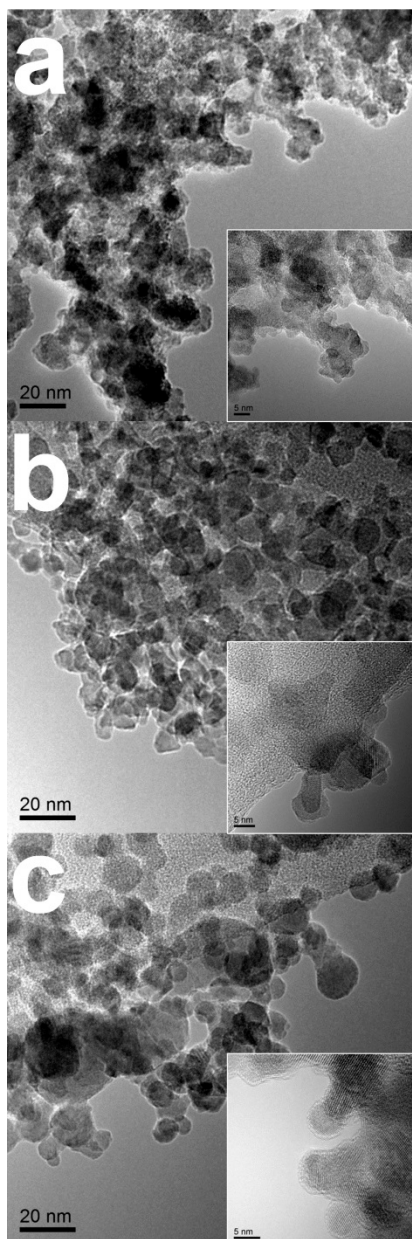


Figure 1. Transmission electron microscopy (TEM) images of (a) PBC; (b) PBCF82; and (c) PBCF55. Each inset shows high-resolution TEM images revealing fringes.

Figure 2 shows the comparison of X-ray diffraction (XRD) patterns of the prepared layered double perovskite catalysts. The comparison of the overall XRD patterns (Figure 2a) of PBC, PBCF82, and PBCF55 reveal peaks that are well indexed to those characteristics of $\text{PrBaCo}_2\text{O}_{6-\delta}$ (P4/mmm) (JCPDS 00-053-0131) with a minor amount of side oxide phases. The broad XRD peaks render convolution of nearby peaks, and confirms the presence of nanoparticles as observed in TEM images. Apart from being in the same crystalline structure, the XRD peaks of PBCF82 and PBCF55 appear at a lower 2-theta value

(Figure 2b) than PBC, which highlights that the perovskite structure exhibits larger lattice parameters upon the incorporation of Fe. The peaks of PBCF55—the one with the most Fe composition—appears at the lowest 2-theta value, suggesting that it exhibits the largest lattice parameters among them. Considering the nature of ordered perovskites, and which cations are oriented in layers, the partial substitution of Co with Fe may lead to B-site cation octahedral tilting, which is difficult to separate from cation ordering [8]. Overall, the comparison of XRD patterns confirms that the layered double perovskite structure is withheld upon Fe incorporation while lattices may expand.

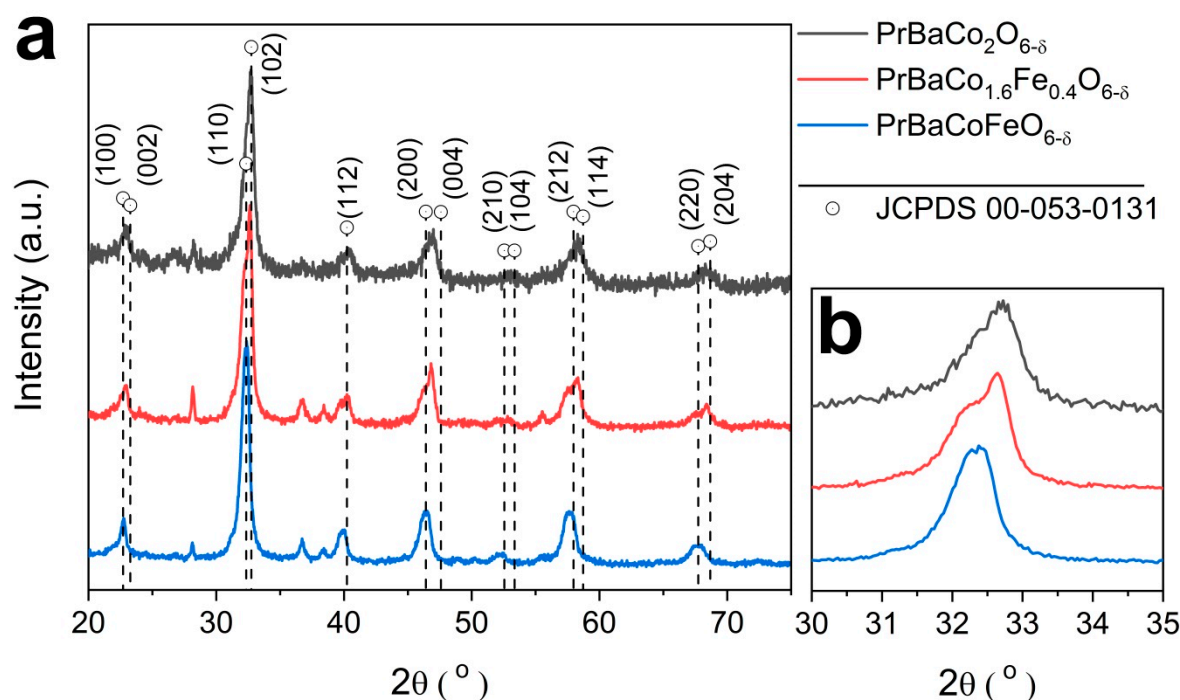


Figure 2. (a) comparison of X-ray diffraction (XRD) patterns of PBC (black), PBCF82 (red), and PBCF55 (blue). The XRD patterns are well indexed to those of $\text{PrBaCo}_2\text{O}_{6-\delta}$ from literature (JCPDS 00-053-0131); (b) magnified view of the main XRD peak.

2.2. Electrochemical Study

Systematic electrochemical characterizations are conducted in order to assess the functional role of Fe in activity and stability of the layered double perovskite catalysts during the OER process. Figure 3a shows constructed Tafel plots from measured steady-state currents from series of chronoamperometry studies of the prepared catalysts. In the presence of Fe, PBCF82 and PBCF55 revealed different Tafel slopes as compared to the non-doped PBC. PBCF82 and PBCF55 both showed similar Tafel slopes ($\sim 50 \text{ mV dec}^{-1}$) that are lower than that of the non-doped PBC (72 mV dec^{-1}) (summarized in Table 1; CVs and steady-state current recorded during the series of chronoamperometry measurement is shown in Figure S1). Our recent study investigated the functional role of Fe in single randomly ordered Co-based perovskites, $\text{Ba}_{0.5}\text{Sr}_{0.5}\text{CoO}_{3-\delta}$ and $\text{La}_{0.2}\text{Sr}_{0.8}\text{CoO}_{3-\delta}$, where remarkable enhancements in their OER activities were reported when doped with $\sim 5 \text{ wt.}\%$ of Fe [24]. However, in this previous study, comparable Tafel slopes were observed for both non-doped and Fe-doped perovskites [24]. In contrast, here, the observed lower Tafel slope indicates that the catalyst would follow a different OER mechanism upon Fe incorporation, which may attribute to certain degree of changes of intrinsic physicochemical properties. PBCF82 and PBCF55 reveal higher current densities at $1.55 \text{ V}_{\text{RHE}}$ (17.1 and 19.7 A g^{-1} , respectively) than compared to the non-doped PBC (13.8 A g^{-1}). Likewise, lower Tafel slopes have been observed for Co based catalysts with increasing Fe composition in other studies [29,31,40]. All of the prepared layer perovskites revealed similar Brunauer–Emmett–Teller (BET) surface areas (Table S1),

which shows that their differences in electrochemical activities are independent of their differences in surface area.

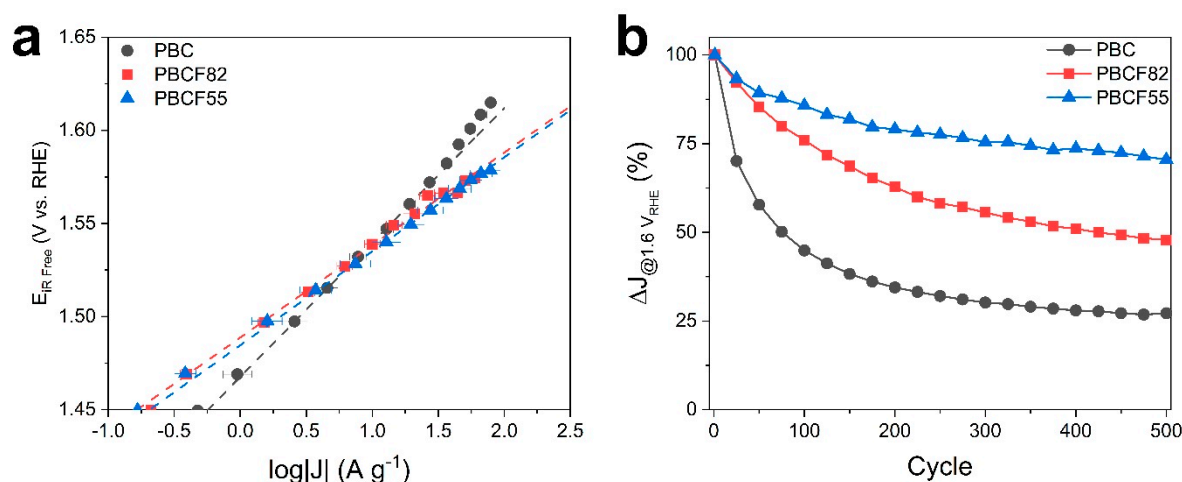


Figure 3. Electrochemical study comparing (a) Tafel plot of oxygen evolution reaction activities and (b) change in current densities with respect to the initial current density at every 25 cycles over 500 cycles between 1.0 and 1.6 V_{RHE} of PBC (black), PBCF82 (red), and PBCF55 (blue).

As previous studies emphasize the importance of understanding the stabilities of electrode materials [2,41–43], the potential stability test was conducted during which steady-state currents are recorded as potential is stepped from 1.0 V_{RHE} to 1.6 V_{RHE} holding for 10 seconds at each potential for 500 cycles (Figure 3b). Here, the Fe-doping also showed a beneficial effect in functional stability where PBCF55 revealed the least amount of current density loss over the period of cycles (lost 32% of its initial current density), while PBC lost about 74%. PBCF82, which comprises less than half of Fe that is in PBCF55, demonstrated capability to retain about half of its initial current density at the end of the cycle (see Table 1). In this comparison, the most outstanding activity and stability are demonstrated by PBCF55 containing one-to-one ratio between Co:Fe in the B-site.

Table 1. Summary of electrochemical study results on oxygen evolution reaction activity and stability: apparent mass specific exchange current density (j_0), Tafel slope (b), activity expressed as mass specific current density at 1.54 V, and stability expressed as percent of initial mass-specific current density after the 500 cycles of stepping between 1.0 V_{RHE} and 1.6 V_{RHE} .

Catalysts	j_0 (A g^{-1})	OER		Stability ΔJ (%)
		Tafel slope (mV dec^{-1})	j @ 1.55 V_{RHE} (A g^{-1})	
PBC	1.47	72	13.8	−73%
PBCF82	1.49	50	17.1	−52%
PBCF55	1.48	50	19.7	−32%

The functional stability of perovskite catalyst is described based on the ability to sustain its initial electrocatalytic activity. In relation to the structural integrity, the catalyst should demonstrate capabilities to serve as a suitable substrate for the prospect of surface oxy(hydroxide) layer formation [24]. In this regard, Pourbaix diagrams are constructed based on density-functional theory (DFT) calculations to assess the thermodynamically stable phases of PBC and PBCF in aqueous solution (Figure S2a,b, respectively). The Pourbaix diagrams of PBC and PBCF suggest the dissolution of A- and B-site cations. In fact, the cation dissolutions of perovskites are pointed out to be inevitable as governed by thermodynamics under the necessary OER conditions [41]. Nevertheless, it is essential to highlight that the degradation mechanism is also driven by kinetics. Hence, each perovskite catalyst

would reach the end of its service life through different pathways based on the defect chemistry under the OER conditions [2,12,43]. In the light of above findings, the incorporation of Fe seems to impede the rate of degradation, where the one with the highest Fe composition (i.e., PBCF55) showed the most enhanced potential stability. Nonetheless, it should be noted that a higher composition of Fe (i.e., Fe-rich; $x > 0.5$) may compromise the role of Co as the active center and intrinsically undergo a different OER mechanism than Co-rich PBCF (i.e., $x < 0.5$) which would dim the assessment of the functional role of Fe-doping [31,40].

2.3. Operando X-ray Absorption Spectroscopy Study

The results of electrochemical studies revealed increasing OER activity and stability with increasing Fe composition in the domain of $0 \leq x \leq 0.5$. As mentioned, $\text{PrBaCo}_{2(1-x)}\text{Fe}_{2x}\text{Co}_{6-\delta}$ with different Co to Fe composition ratios would follow different reaction pathways as they undergo different degradation processes under the OER condition. Therefore, operando X-ray absorption spectroscopy study is conducted in order to monitor the changes in local electronic and geometric structures of the prepared layered double perovskites during the OER process, through which the functional effects of Fe were highlighted.

In Figure 4a, Co K-edge energy positions of normalized X-ray absorption near edge structure (XANES) spectra of as-prepared double perovskites reveal that PBC and PBCFs have Co oxidation state between +2 and +3, for which the Co K-edge position of PBCF55 is positioned at the lowest energy level. Through comparison, $\text{PrBaCo}_{2(1-x)}\text{Fe}_{2x}\text{Co}_{6-\delta}$ show reduced Co oxidation states with increasing Fe composition (i.e., x) in the following descending order: PBC > PBCF82 > PBCF55, each with ~ 0.3 eV difference in their Co K-edge energy position. With this information, the concentration of oxygen vacancy can be relatively estimated as listed in ascending order: PBC < PBCF82 < PBCF55 (refer to Figure S3). Note that all edge energy positions were determined at the half of the edge step. Figure 4b shows the comparison of the Fourier-transformed (FT) k^3 -weighted Co K-edge extended X-ray absorption fine structure (EXAFS) spectra of as-prepared PBC, PBCF82, and PBCF55. The peaks of FT-EXAFS spectra signify the presence of neighboring atomic shells at specific radial distances from the absorbing atom (i.e., Co). In Figure 4b, the first two major peaks at ~ 1.9 Å and ~ 2.8 Å are ascribable to the backscattering contributions from the nearest Co–O and Co–Co/Fe ligands, respectively. Here, it is noteworthy that the second peak is ascribable to Co–Co/Fe coordination shell of the edge-sharing polyhedra typically found in highly oxygen deficient perovskite oxides prepared by flame spray synthesis (see Figure S2) [2,44,45]. Inconveniently, this Co–Co/Fe ligand distance of edge-sharing polyhedra of $\text{PrBaCo}_{2(1-x)}\text{Fe}_{2x}\text{Co}_{6-\delta}$ is in close vicinity to that of Co/Fe-oxy(hydroxide) (refer to Supplementary Information S5 for detailed explanation). The next appearing peaks located at ~ 3.5 Å corresponds to Pr/Ba neighbors. All of the FT-EXAFS profiles of PBC, PBCF82, and PBCF55 show similar peak locations to one another, suggesting that a similar local structure is maintained upon Fe incorporation. In Figure 4b, the first peak amplitude is observed to be decreased in the presence of Fe; listed in the descending order of amplitude: PBC > PBCF82 > PBCF55. Given that the first peak is ascribable to Co–O coordination shell, Co of the layered double perovskite seems to be bound to less oxygen atoms at that radial distance in the presence of Fe. This is further verified by the best fit of the Co–O peak of FT-EXAFS spectra of as-prepared catalysts, which shows the decrease in Co–O coordination number with a higher amount of Fe-doping (refer to Figure S10). Together with the comparison of XANES spectra, these findings lead to assert that more oxygen vacant sites are created with a higher amount of Fe-doping, and therefore reduces Co oxidation state in $\text{PrBaCo}_{2(1-x)}\text{Fe}_{2x}\text{Co}_{6-\delta}$. Moreover, the decrease of scattering intensities at farther radial distances observed in the FT-EXAFS spectra of both PBCF82 and PBCF55 is rationalized by octahedral distortions induced by doping of Fe (+3) into the B-site replacing Co ($\sim +2.7$) cations, which then weakens the backscattering from the neighboring atoms [35,46–53].

Furthermore, Figure 4c,d display comparisons of normalized XANES and FT-EXAFS spectra, respectively, of PBCF82 and PBCF55 recorded at the Fe K-edge. In Figure 4c, the edge energy positions

of Fe K-edge XANES spectra of PBCF82 and PBCF55 indicates that their Fe oxidation states are similar (between +3 and +4). More precisely, the Fe K-edge of PBCF55 is positioned at about ~0.1 eV lower energy than PBCF82, but this insignificant difference would make the comparison trivial. Figure 4d shows Fe K-edge FT-EXAFS spectra of both PBCF82 and PBCF55 with similar scattering patterns as those of Co K-edge FT-EXAFS spectra. This confirms that Fe is indeed well integrated into the B-site of perovskite structure.

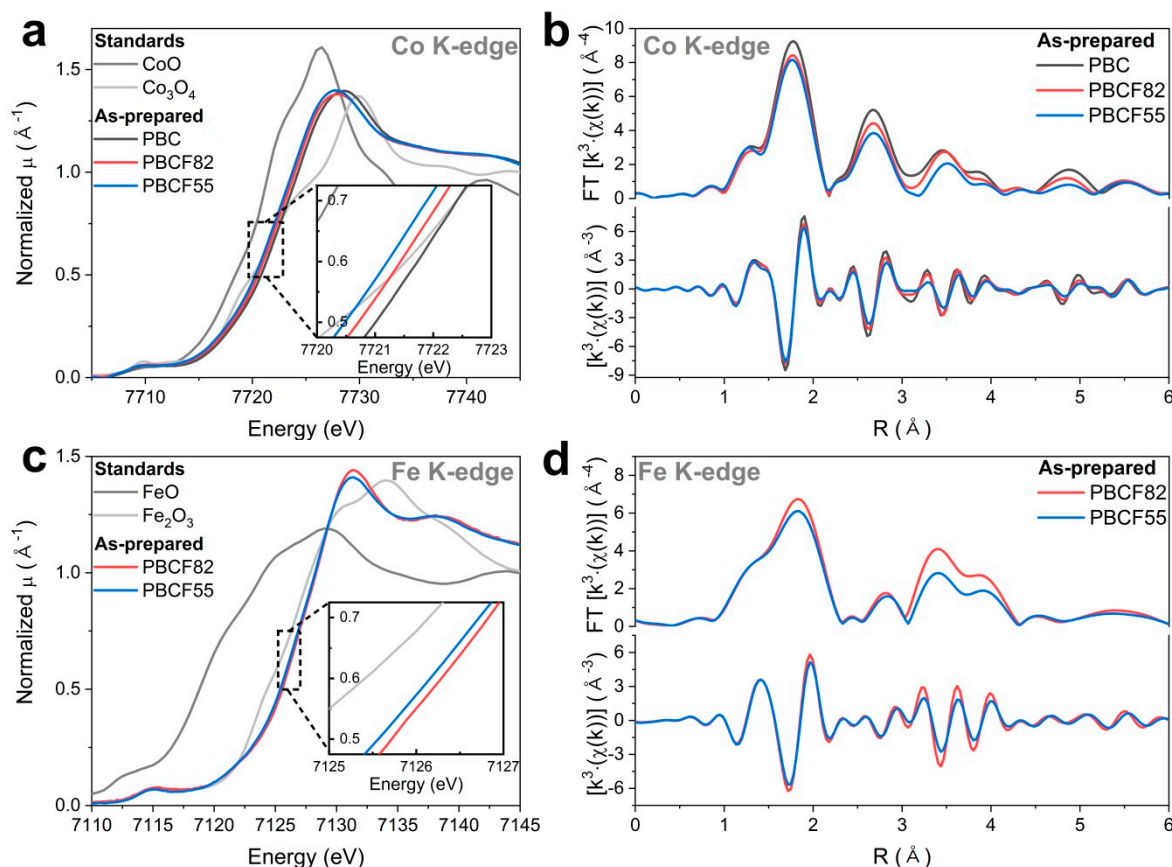


Figure 4. Comparison of as-prepared PBC, PBCF82, and PBCF55 Co K-edge (a) X-ray absorption near edge spectra (XANES) spectra; (b) Fourier-transformed extended X-ray absorption fine structure (FT-EXAFS) spectra; and Fe K-edge: (c) XANES spectra; and (d) FT-EXAFS spectra.

When a neutral oxygen vacancy is created during synthesis, the left behind electrons would be distributed to either to Co and/or Fe, which would lower their oxidation states. However, the electrons are not evenly distributed among them but rather more accepted by Fe [40,48]. Based on above evidence, the addition of Fe seems to aid Co to be stable in a lower oxidation state by providing charge stabilization through balancing oxygen non-stoichiometry, and therefore promotes formation of oxygen vacancies. In the presence of higher oxygen vacancy concentration, the lattice oxygen within the perovskite structure is more inclined to participate in the water oxidation reaction (i.e., LOER) and develops the OER active oxy(hydroxide) layer at the surface [3,27].

Figure 5a shows a shift of the Co K-edge XANES spectra to higher energy positions of PBC, PBCF82, and PBCF55 during the operando flow cell test, among which PBCF55 reveals the greatest extent of energy shift of ~0.7 eV at the highest potential, while PBC and PBCF82 display ~0.3 eV of edge shifts. Our previous studies showed that the positive Co K-edge shift during the OER process is attributed to the construction of the OER active oxy(hydroxide) layer, since the Co oxidation state of Co-oxy(hydroxide) layer is higher than those inherent in the perovskite oxide [2,27]. This also agrees with other DFT based studies [46,47,51]. Therefore, revisiting Figure 3a, the high OER activity of

PBCF55 can be explained by the large extent of increase in the Co oxidation state reading from the shift of the Co K-edge position. At this point, we emphasize that the rate of dissolution (i.e., degradation) of a perovskite oxide catalyst during the OER process is controlled by its kinetics; thereby, each catalyst would reach its end-of-service life at a different rate. In this context, Figure 5b shows Co K-edge shifts at each increasing applied potential with respect to the energy positions recorded at 1.2 V_{RHE} during the anodic polarization in flow cell test. In Figure 5b, Fe-doped PBCF82 and PBCF55 reveal rapid positive Co K-edge shifts when polarized into the oxygen evolution regime (> 1.4 V_{RHE}). The edge shift translates proportionally to the increase of Co oxidation state. This sudden increase of Co oxidation state when polarized above the OER onset signifies formation of the OER active oxy(hydroxide) layer, which is potential-induced. Meanwhile, in the absence of Fe, PBC shows a consistent increase even at potentials below the oxygen evolution regime, indicating that the oxidation of its Co species is triggered by chemical dissolution [2].

Particularly, even though the extent of Co K-edge shift of PBCF82 is smaller than that of PBCF55, PBCF82 demonstrated a similar OER activity as PBCF55. Nevertheless, PBCF82 showed a rapid yet subtle increase of the Co oxidation state when polarized above the OER onset as similar to PBCF55 (Figure 5b). This may suggest the development of Co oxy(hydroxide) layer occurs but still less than in the case of PBCF55. Based on these observations, PBCF82 and PBCF55 both show different Co oxidation behaviors than compared to PBC, suggesting that the catalyst would undergo a modified degradation pathway during the OER process upon Fe incorporation. Referring to the Tafel plot (Figure 3a), the difference in their Tafel slopes, where lower Tafel slopes are observed upon Fe-doping, may suggest that PBCF's would undergo different mechanism during OER than the non-doped PBC. Also referring to the stability test (Figure 3b), the inhibited degradation mechanism upon Fe incorporation is further supported by the improved current stabilities of PBCF82 and PBCF55. Although thermodynamics anticipate the dissolution of $\text{PrBaCo}_{2(1-x)}\text{Fe}_{2x}\text{Co}_{6-\delta}$, it is intriguing to observe an enhanced ability to retain the initial current density upon Fe-doping, where PBCF55 demonstrated the highest retention of current density over the course of 500 cycles. The above findings point out that Fe plays an important role in improving the stability owing to the retardation of degradation mechanism, where the potential-induced increase of Co oxidation state is more attributable to the development of Co-oxy(hydroxide) species. However, this does not mean that deterioration of the perovskite structure is completely avoided as the decreasing trend of current densities are observed during the stability test. In brief, while the rate of chemical dissolution is lagged upon the addition of Fe, the layered double perovskite can be sustained as a substrate for the development of OER active oxy(hydroxide) species.

Despite the clear indications as to which the construction of Co-oxy(hydroxide) is displayed by positive edge shifts in their Co K-edge XANES spectra, this development—along with other concurrent local structural changes—are not clearly manifested in the comparison of FT-EXAFS spectra collected at potentials below and above the OER onset (1.2 and 1.54 V_{RHE}, respectively) (Figure S6a–c). Here, it is important to recapitulate the coinciding Co–Co radial distances between the edge-sharing polyhedra of $\text{PrBaCo}_{2(1-x)}\text{Fe}_{2x}\text{Co}_{6-\delta}$ and that of the Co-oxy(hydroxide) layer, both of which are at the proximity of ~2.8 Å from their primary Co atoms. In this respect, the FT-EXAFS profiles with these concurring signals would confound the precise interpretation of local structural changes. Considering these challenges, only the first peak is fitted in order to verify the changes in the Co–O coordination during the OER process (summarized in Table S3 and Figure S10). The best fits show increased Co–O coordination numbers for all catalysts at the highest anodic potential (1.54 V_{RHE}) and therefore further consolidates the increase of Co oxidation states during the OER process.

While the increase of Co oxidation states is evident, Fe K-edge XANES spectra collected during the operando measurement (Figure 5c) reveal insignificant edge shifts (~0.1 eV) throughout the course of anodic polarization. The Fe in both PBCF82 and PBCF55 are in a higher oxidation state (between +3 and +4) than Co (< +2.7), which allows Co to be in a more reduced state and thereby being more flexible in accommodating charge transfers [48]; this justifies the insignificant shift in the Fe K-edge.

In this context, the formation of the active oxy(hydroxide) layer would therefore be accommodated more by Co polyhedra, and thereby less changes would be manifested in their Fe K-edge FT-EXAFS profiles (Figure S6).

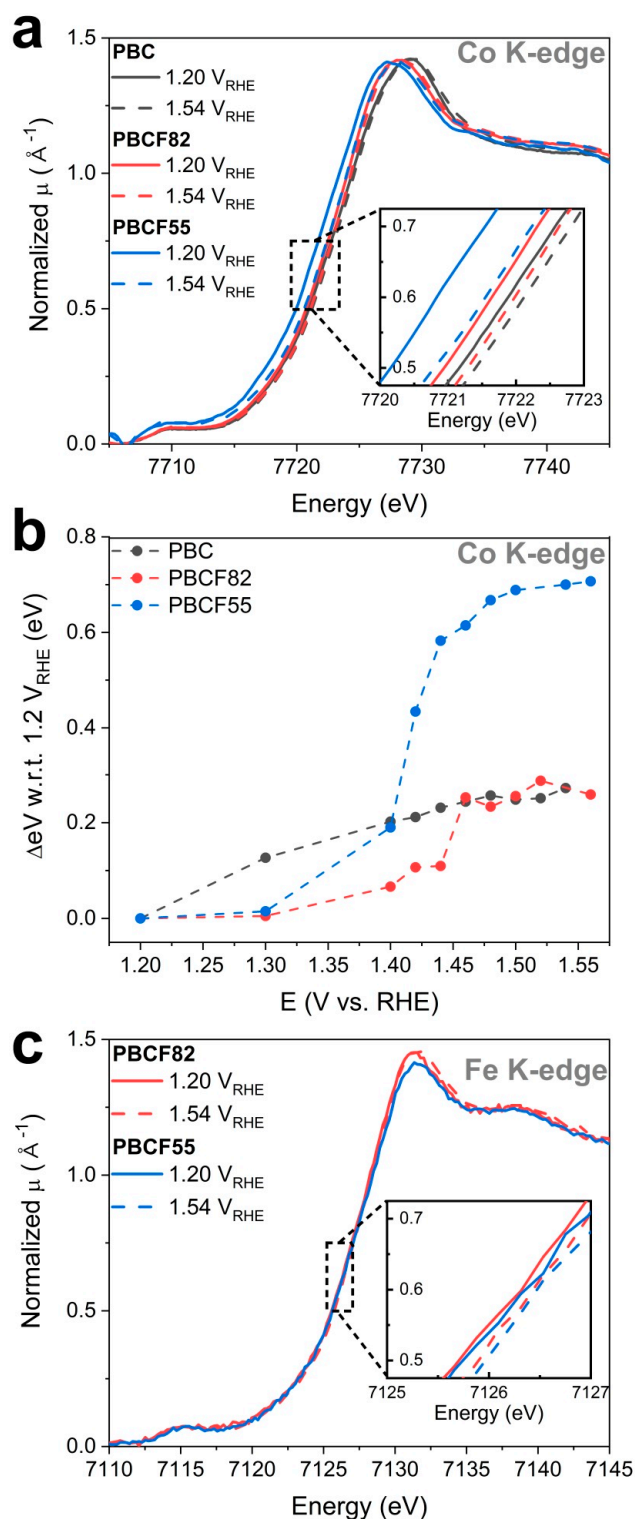


Figure 5. (a) comparison of Co K-edge XANES spectra of PBC, PBCF82, and PBCF55 recorded at 1.2 and $1.54 V_{\text{RHE}}$; and (b) Co K-edge energy shift measured with respect to the edge position at $1.2 V_{\text{RHE}}$ at each potential during operando flow cell tests; (c) comparison of Fe K-edge XANES spectra of PBCF82 and PBCF55 recorded at 1.2 and $1.54 V_{\text{RHE}}$.

In light of our findings, the Fe incorporation into the layered double perovskite catalyst leads to stabilizing Co in a lower oxidation state by providing a better charge distribution and promoting the formation of oxygen vacancies. Consequently, the degradation mechanism is inhibited such that the oxidation of Co is more induced by the increase of potential while its chemical dissolution is decelerated yet still unavoidable. The potential-induced Co oxidation behavior upon Fe-doping is indicative of the development of the OER active Co-oxy(hydroxide) surface layer. Despite these enhancements, no significant electronic and structural changes were detected with respect to Fe. Overall, the addition of Fe seems to enable the layered double perovskite catalyst to improve its structural integrity (similar as previously observed for $\text{Ni}_x\text{Fe}_{1-x}\text{O}_2$) [37] as a more suitable substrate for the construction of oxy(hydroxide) layer leading to enhanced OER activity and stability.

3. Materials and Methods

3.1. Material Synthesis

The flame spray synthesis setup is described by Heel et al [54]. For the preparation of the $\text{PrBaCo}_2\text{O}_{5+x}$ (PBC) and $\text{PrBaCo}_{2-y}\text{Fe}_y\text{O}_{5+x}$ ($y = 0.4$ and 1.0) precursor solutions, stoichiometric amounts of praseodymium oxide (Pr_6O_{11} , 99.9%, Auer Remy, Hamburg, Germany), barium carbonate (BaCO_3 , $\geq 99\%$, Sigma-Aldrich, Darmstadt, Germany), cobalt nitrate hexahydrate ($\text{Co}(\text{NO}_3)_2 \cdot 6\text{H}_2\text{O}$, 99.9%, Sigma-Aldrich, Darmstadt, Germany) and iron nitrate nonahydrate ($\text{Fe}(\text{NO}_3)_3 \cdot 9\text{H}_2\text{O}$, $\geq 98\%$, Sigma-Aldrich, Darmstadt, Germany) were dissolved in a mixture of solvents composed by *N,N*-Dimethylformamide (DMF, $\geq 99.8\%$, Roth, Frankfurt, Germany), acetic acid (HAc, $\geq 99.0\%$, Sigma-Aldrich, Darmstadt, Germany), nitric acid (HNO_3 , 70%, Sigma-Aldrich, Darmstadt, Germany) and water in 45:25:5:25 volume ratio, respectively. Firstly, the Pr_6O_{11} was dissolved in the mixture of water and nitric acid at 80°C ; when a clear green solution was obtained, the BaCO_3 was added and then, when no more CO_2 bubbles were observed, the Co and Fe (only for PBCF solutions) metal precursors. When all dissolved, the HAc and the DMF were added, obtaining a final total metal concentration of 0.1 M. The precursor solutions were pumped into the flame by using a three piston pump (C-601, Büchi, Flawil, Switzerland) with a flow controller (C-610, Büchi, Flawil, Switzerland), using a constant flow free of pulsations of 20 mL min^{-1} . Pure oxygen (99.95%, Carbagas, Bern, Switzerland) was used as dispersion gas with a flow rate of 35 L min^{-1} . The combustion gas was formed by acetylene (99.6%, Carbagas, Bern, Switzerland), with a flow rate of 13 L min^{-1} , and pure oxygen (17 L min^{-1}). Finally, the powders were collected in a baghouse filter on four ashless paper filters (Whatman, Buckinghamshire, UK).

3.2. Material Characterizations

Phase characterization of prepared materials was performed using powder X-ray diffraction (XRD, Bruker (Billerica, MA, USA) D8 system in Bragg–Brentano geometry, Cu K- α radiation ($\lambda = 0.15418\text{ nm}$)). Specific surface area was calculated by Brunauer–Emmett–Teller (BET) analysis of N_2 adsorption/desorption isotherms (AUROSORB-1, Quantachrome, Boynton Beach, FL, USA). Transmission electron microscopy (TEM) and energy dispersive X-ray spectroscopy (EDX) (TECNAI F30 operated at 300 kV) were used to study the surface morphology and composition of the prepared materials.

For ex situ and operando X-ray absorption spectroscopy (XAS) measurements, catalyst powders were dispersed in a mixture of isopropanol and Milli-Q water in the equal ratio sonicated for 30 min. The ink was then spray coated on Kapton film. XAS spectra at the Co K-edge and Fe K-edge were recorded at the SuperXAS beamline of the Swiss Light Source (PSI, Villigen, Switzerland). The incident photon beam provided by a 2.9 T superbend magnet source was collimated by a Si-coated mirror at 2.5 mRad (which also served to reject higher harmonics) and subsequently monochromatized by a Si (111) channel-cut monochromator. A Rh-coated toroidal mirror at 2.5 mRad was used to focus the X-ray beam to a spot size of 1 mm by 0.2 mm maximal on the sample position. The SuperXAS beamline [55]

allowed for the rapid collection of 120 spectra during a measurement time of 60 sec (QEXAFS mode), which were then averaged. The spectra of samples were collected in transmission mode using N₂ filled ionization chambers, where a Co foil (of Fe foil) was placed between the second and third ionization chamber as a reference to calibrate and align collected spectra. Extended X-ray absorption fine structure (EXAFS) spectra were analyzed using the Demeter software package (0.9.26, Bruce Ravel, Washington D.C., USA) [56], which included background subtraction, energy calibration (based on the simultaneously measured Co reference foil) and edge step normalization. The resulting spectra were converted to the photoelectron wave vector k (in units \AA^{-1}) by assigning the photoelectron energy origin, E_0 , corresponding to $k = 0$, to the first inflection point of the absorption edge. The resulting $\chi(k)$ functions were weighted with k^3 to compensate for the dampening of the EXAFS amplitude. These $\chi(k)$ functions were Fourier transformed over 3–12 \AA^{-1} and plotted. The scattering paths used for the EXAFS fittings of all catalysts were generated from the structure of CoOOH [57] for the first Co–O coordination shell using the FEFF6.2 library. Refer to Supplementary Information S6 for detailed description of FT-EXAFS fittings.

3.3. Electrochemical Characterization

The electrochemical activities of the prepared catalysts were evaluated in a standard three-electrode electrochemical cell with the thin-film rotating disk electrode (RDE) [58]. The setup for OER and cyclic voltammetry (CV) consists of a potentiostat (Biologic VMP-300, Cary, NC, USA) and a rotation speed controlled motor (Pine Instrument Co., AFMSRCE, Grove City, PA, USA). All the electrochemical measurements were performed at standard room temperature using a reversible hydrogen electrode (RHE) as the reference electrode in 0.1 M KOH. A gold mesh was used as the counter electrode. A Teflon cell was used to contain the electrolyte with the electrodes immersed under potential control. A porous thin film electrode was prepared by drop-casting a catalyst ink on a polished glassy carbon electrode (5 mm OD/0.196 cm²) [58]. The catalyst ink was prepared from a catalyst suspension made from sonicating (Bandelin, RM 16 UH, 300 Weff, 40 kHz, Berlin, Germany) 10 mg of catalyst in a solution mixture of 4 mL isopropyl alcohol (Sigma-Aldrich, 99.999%, Darmstadt, Germany) and 1 mL of Milli-Q water (ELGA, PURELAB Chorus, High Wycombe, UK), and 20 μL of Na⁺-exchanged Nafion [4]. The 0.1 M KOH electrolyte was prepared by dissolving KOH pellets (Sigma-Aldrich, 99.99%, Darmstadt, Germany) in Milli-Q water.

First, 25 reverse potentiostatic sweeps of CV were conducted in synthetic air-saturated electrolyte from 1.0 to 1.7 V_{RHE} at a scan rate of 10 mV s^{−1}. Then, chronoamperometric measurements were carried out holding each potential step for 30 seconds to obtain steady-state currents at each potential from 1.2 to 1.7 V_{RHE} while rotating the working electrode at 900 rpm. The potential stability of catalyst materials was conducted using the same setup, by stepping potential between 1.0 and 1.6 V_{RHE} 500 times holding 10 seconds at each potential to collect currents at steady-state. Five cycles of CV and electrochemical impedance spectroscopy (EIS) were carried out after every 100 cycles. All measured currents were normalized by the mass of catalyst loading, and potentials were corrected for the ohmic drop obtained from EIS.

3.4. Operando Flow Cell Study

The homemade operando XAS electrochemical flow cell used in this study was extensively described previously [59]. As explained in Section 3.2, electrode materials were spray coated at the center of Kapton films. Black pearl-2000 (Cabot Corp., Boston, MA, USA) was used as the counter electrode material. A silver chloride electrode (Ag⁺/AgCl) (Hugo Sachs Elektronik, March, Germany) was used as the reference electrode. During electrochemical testing, the electrolyte was drawn into the cell and collected in a syringe at the flow rate of 0.1 mL min^{−1}. The chronoamperometry measurement was carried out holding for 120 sec at each anodic potential step from 1.2 V_{RHE} to 1.54 V_{RHE} , and again during the reverse sequence back to 1.2 V_{RHE} . At each potential step, both transmission XAS spectra at

the Co and Fe K-edges were collected simultaneously for 60 seconds. The energy position of Co and Fe K-edge were read with respect to the half of the edge-step.

3.5. Density-Functional Theory—Pourbaix Diagrams

Density-functional theory (DFT) calculations are used to help understand the experimental data. In the first set of calculations, the stability of the perovskites in an aqueous environment was investigated by means of Pourbaix diagrams. This method has been previously used to investigate the stability of Ru-based perovskites in water as a descriptor for the stability in water to identify novel light harvesting materials [60]. Pourbaix diagrams show the phase diagram of solid and dissolved species as a function of pH and applied potential (V_{SHE}). DFT provides the total energies for the solid bulk for the perovskites and the other solid competing phases as described in the Materials Project database [61]. Experiments provide the dissolution energies for the dissolved species [62,63]. This method is implemented in the Atomic Simulation Environment (ASE) package [64], and more details about the methodology can be found in the literature [65,66]. All the bulk structures have been fully relaxed using the Quantum ESPRESSO code [67], PBEsol as exchange-correlation functional [68] and the pseudopotentials from the Standard Solid State Pseudopotential library (SSSP accuracy) [69]. We used Hubbard U+ correction of 4 eV and applied to Co, Fe, and Pr elements.

4. Conclusions

In here, a systematic study is conducted to assess the role of Fe in the highly OER active layered double perovskite catalyst, $\text{PrBaCo}_{2(1-x)}\text{Fe}_{2x}\text{Co}_{6-\delta}$, by comparing different compositions of Fe: PBC ($x = 0$), PBCF82 ($x = 0.2$), and PBCF55 ($x = 0.5$). These layered double perovskite catalysts are prepared via flame spray synthesis, where Fe is indeed incorporated into the B-site as verified by XRD and FT-EXAFS profiles. In comparison to PBC, Fe-doped PBCF82 and PBCF55 revealed enhanced OER activities and improved current stabilities as to better retain the initial current density. In the basis of our findings, such enhanced electrocatalytic performance is attributed to the addition of Fe, which provides charge stability as to compensate for the oxygen non-stoichiometry and allows Co to be in a lower oxidation state. This leads to alteration in the oxidation behavior of the layered double perovskite catalyst upon anodic polarization so that its Co oxidation is predominantly provoked by the increase of applied potential. In addition, the potential-induced Co oxidation upon Fe-doping is attributed to the formation of OER active oxy(hydroxide) layer at the surface. This also implies that the perovskite structure is prolonged under the OER conditions so that it serves as a substrate longer for the construction of oxy(hydroxide) layer at the surface. It should be noted that, even in the presence of Fe, the catalyst is not exempted from the inevitable cation dissolution under the OER conditions as governed by its thermodynamic nature. All of these effects lead to highlighting the constructive role of Fe in the layered double perovskite as an OER catalyst, which is evident from lower Tafel slopes and enhanced current density stabilities of PBCF82 and PBCF55. Particularly, PBCF55—with the highest Fe composition—demonstrated the greatest enhancement in both activity and stability as OER catalyst.

In summary, these results lead to concluding that a layered double perovskite catalyst is intrinsically modified upon Fe-doping so that it becomes more resilient to the cation dissolution, and thereby better supports the development of an oxy(hydroxide) surface layer. Such changes contribute to enhancements in the activity towards oxygen evolution reaction. As conventionally seen from many transition metal oxide catalysts, such electrocatalytic performance enhancements are attributed to the synergy between Fe and Co. In this regard, it should be emphasized that the incorporation of Fe would modify the degradation mechanism of the host transition metal. Thus, it should be generalized that the electrocatalytic performance of a doped-metal oxide would rely on the interaction between the host transition metal and the dopant metal. These findings present a systematic study method to engineer and design an ideal perovskite oxide as OER catalyst.

Supplementary Materials: The following are available online at <http://www.mdpi.com/2073-4344/9/3/263/s1>, Figure S1: The initial cyclic voltammetry scanned at 10 mV sec^{−1} from 1.0 to 1.7 V_{RHE}, and the series of chronoamperometry measurements recording steady-state current at each step of potential: (a–b) PBC; (c–d) PBCF82; and (e–f) PBCF55; Figure S2: Density-functional theory (DFT) calculated Pourbaix diagrams of (a) PrBaCo₂O_{6-δ} and (b) PrBaCo_{2(1-x)}Fe_{2x}O_{6-δ} (i.e., PBCF82 and PBCF55). Red lines mark the ranges of the working potential (on standard hydrogen electrode (SHE) potential scale) for the oxygen evolution reaction (OER) in at pH 13 used during the operando XAS study; Figure S3: Comparison of XANES spectra of PBC prepared via sol-gel (SG) method (black) and PBC (red), PBCF82 (blue), and PBCF55 (green) prepared via flame spray synthesis; Figure S4: Illustration of Co–Co distances in (a) Co octahedra, surrounded by six oxygen atoms in an octahedral structure sharing a single oxygen corner in a typical stoichiometric perovskite (ABO₃/A'A''B'B''O₆); and (b) B-site cation surrounded by less oxygen than stoichiometry (ABO_{3-δ}/A'A''B'B''O_{6-δ}); therefore, the network of polyhedra would stabilize by pivoting to share two oxygen atoms; Figure S5: Comparison of Fourier transformed (FT) k³-weighted EXAFS profiles at Co K-edge of γ-Co-O(OH) [3] with as-prepared layered double perovskite catalysts: PBC (black), PBCF82 (red), and PBCF55 (blue); Figure S6: Comparison of FT Co K-edge EXAFS spectra collected at 1.20 and 1.54 V_{RHE} during the operando XAS measurements of (a) PBC, (b) PBCF82, and (c) PBCF55. Simultaneously collected Fe K-edge EXAFS spectra of (d) PBCF82 and (e) PBCF55; Figure S7: Fourier transformed k₃-weighted Co K-edge EXAFS spectra of PBC (a) as-prepared, (b) at 1.2 V_{RHE} anodic, and (c) 1.54 V_{RHE} anodic. Black line is the FT-EXAFS spectrum, red line is the fitted spectrum, and blue is the window of the fitting; Figure S8: Fourier transformed k₃-weighted Co K-edge EXAFS spectra of PBCF82 (a) as-prepared, (b) at 1.2 V_{RHE} anodic, and (c) 1.54 V_{RHE} anodic. Black line is the FT-EXAFS spectrum, red line is the fitted spectrum, and blue is the window of the fitting; Figure S9: Fourier transformed k₃-weighted Co K-edge EXAFS spectra of PBCF55 (a) as-prepared, (b) at 1.2 V_{RHE} anodic, and (c) 1.54 V_{RHE} anodic. Black line is the FT-EXAFS spectrum, red line is the fitted spectrum, and blue is the window of the fitting; Figure S10: Comparison of coordination number (N_{Co–O}) of the first peak of FT-EXAFS spectra of PBC (black), PBCF82 (red), and PBCF55 (blue). Filled markers and empty markers represent N_{Co–O} of the as-prepared catalysts and at 1.54 V_{RHE} during the anodic polarization, respectively; Table S1: Summary of Brunauer–Emmet–Teller (BET) surface areas of the prepared layered double perovskite catalysts; Table S2: Lattice parameters of PBC, PBCF82, and PBCF55 calculated from Rietveld refinement of their X-ray diffractions. With the estimated lattice parameter, the Co–Co distance of edge-sharing polyhedron is calculated; Table S3: Summary of best fit parameters of the FT k₃-weighted Co K-edge EXAFS spectra of as-prepared and at 1.20 and 1.54 V_{RHE} during the anodic polarization of (a) PBC, (b) PBCF82, and (c) PBCF55.

Author Contributions: Conception and conceptualization, B.-J.K., E.F., and T.J.S.; synthesis, M.B. and T.G.; characterizations, electrochemical measurements, and investigation, B.-J.K.; DFT computations, I.E.,C.; B.-J.K., E.F., I.E.,C., M.B., T.G., M.N. and T.J.S. discussed the results and commented on the manuscript.

Funding: This research was funded by Swiss National Science Foundation, Innosuisse and the Swiss Competence Center for Energy Research (SCCER) Heat and Paul Scherrer Institute.

Acknowledgments: The authors gratefully acknowledge the Swiss National Science Foundation through its Ambizione Program and the National Centre of Competence in Research (NCCR) Marvel, the Swiss Competence Center for Energy Research (SCCER) Heat and Electricity Storage through Innosuisse, Switzerland, and the Paul Scherrer Institute for financial contributions to this work, respectively. The authors thank the Swiss Light Source for providing beamtime at the SuperXAS beamline.

Conflicts of Interest: The authors declare no conflict of interest.

References

1. Babic, U.; Suermann, M.; Buehi, F.N.; Gubler, L.; Schmidt, T.J. Review-identifying critical gaps for polymer electrolyte water electrolysis development. *J. Electrochem. Soc.* **2017**, *164*, F387–F399. [CrossRef]
2. Kim, B.-J.; Cheng, X.; Abbott, D.F.; Fabbri, E.; Bozza, F.; Graule, T.; Castelli, I.E.; Wiles, L.; Danilovic, N.; Ayers, K.E.; et al. Highly active nanoperovskite catalysts for oxygen evolution reaction: Insights into activity and stability of Ba_{0.5}Sr_{0.5}Co_{0.8}Fe_{0.2}O_{2+δ} and PrBaCo₂O_{5+δ}. *Adv. Funct. Mater.* **2018**, *28*, 1804355. [CrossRef]
3. Cheng, X.; Fabbri, E.; Yamashita, Y.; Castelli, I.E.; Kim, B.; Uchida, M.; Haumont, R.; Puente-Orench, I.; Schmidt, T.J. Oxygen evolution reaction on perovskites: A multieffect descriptor study combining experimental and theoretical methods. *ACS Catal.* **2018**, *8*, 9567–9578. [CrossRef]
4. Suntivich, J.; Gasteiger, H.A.; Yabuuchi, N.; Shao-Horn, Y. Electrocatalytic measurement methodology of oxide catalysts using a thin-film rotating disk electrode. *J. Electrochem. Soc.* **2010**, *157*, B1263–B1268. [CrossRef]
5. Grimaud, A.; May, K.J.; Carlton, C.E.; Lee, Y.L.; Risch, M.; Hong, W.T.; Zhou, J.G.; Shao-Horn, Y. Double perovskites as a family of highly active catalysts for oxygen evolution in alkaline solution. *Nat. Commun.* **2013**, *4*, 2439. [CrossRef] [PubMed]
6. Huang, X.B.; Zhao, G.X.; Wang, G.; Irvine, J.T.S. Synthesis and applications of nanoporous perovskite metal oxides. *Chem. Sci.* **2018**, *9*, 3623–3637. [CrossRef] [PubMed]

7. Hwang, J.; Rao, R.R.; Giordano, L.; Katayama, Y.; Yu, Y.; Shao-Horn, Y. Perovskites in catalysis and electrocatalysis. *Science* **2017**, *358*, 751–756. [[CrossRef](#)] [[PubMed](#)]
8. Vasala, S.; Karppinen, M. A2b'b''o6 perovskites: A review. *Prog. Solid State Chem.* **2015**, *43*, 1–36. [[CrossRef](#)]
9. Fabbri, E.; Habereder, A.; Waltar, K.; Kotz, R.; Schmidt, T.J. Developments and perspectives of oxide-based catalysts for the oxygen evolution reaction. *Catal. Sci. Technol.* **2014**, *4*, 3800–3821. [[CrossRef](#)]
10. King, G.; Woodward, P.M. Cation ordering in perovskites. *J. Mater. Chem.* **2010**, *20*, 5785–5796. [[CrossRef](#)]
11. Davies, P.K.; Wu, H.; Borisevich, A.Y.; Molodetsky, I.E.; Farber, L. Crystal chemistry of complex perovskites: New cation-ordered dielectric oxides. *Annu. Rev. Mater. Res.* **2008**, *38*, 369–401. [[CrossRef](#)]
12. Fabbri, E.; Schmidt, T.J. Oxygen evolution reaction—the enigma in water electrolysis. *ACS Catal.* **2018**, *8*, 9765–9774. [[CrossRef](#)]
13. Grimaud, A.; Diaz-Morales, O.; Han, B.H.; Hong, W.T.; Lee, Y.L.; Giordano, L.; Stoerzinger, K.A.; Koper, M.T.M.; Shao-Horn, Y. Activating lattice oxygen redox reactions in metal oxides to catalyze oxygen evolution. *Nat. Chem.* **2017**, *9*, 457–465. [[CrossRef](#)] [[PubMed](#)]
14. Taskin, A.A.; Lavrov, A.N.; Ando, Y. Achieving fast oxygen diffusion in perovskites by cation ordering. *Appl. Phys. Lett.* **2005**, *86*, 091910. [[CrossRef](#)]
15. Kim, G.; Wang, S.; Jacobson, A.J.; Yuan, Z.; Donner, W.; Chen, C.L.; Reimus, L.; Brodersen, P.; Mims, C.A. Oxygen exchange kinetics of epitaxial prbaco(2)o(5+delta) thin films. *Appl. Phys. Lett.* **2006**, *88*. [[CrossRef](#)]
16. Man, I.C.; Su, H.Y.; Calle-Vallejo, F.; Hansen, H.A.; Martinez, J.I.; Inoglu, N.G.; Kitchin, J.; Jaramillo, T.F.; Nørskov, J.K.; Rossmeisl, J. Universality in oxygen evolution electrocatalysis on oxide surfaces. *ChemCatChem* **2011**, *3*, 1159–1165. [[CrossRef](#)]
17. Rossmeisl, J.; Qu, Z.W.; Zhu, H.; Kroes, G.J.; Nørskov, J.K. Electrolysis of water on oxide surfaces. *J. Electroanal. Chem.* **2007**, *607*, 83–89. [[CrossRef](#)]
18. Damjanovic, A.; Jovanovic, B. Anodic oxide-films as barriers to charge-transfer in o2 evolution at pt in acid solutions. *J. Electrochem. Soc.* **1976**, *123*, 374–381. [[CrossRef](#)]
19. Han, B.; Shao-Horn, Y. (invited) in-situ study of the activated lattice oxygen redox reactions in metal oxides during oxygen evolution catalysis. *Meeting Abstracts* **2018**, MA2018-01, 1935.
20. Yoo, J.S.; Rong, X.; Liu, Y.; Kolpak, A.M. Role of lattice oxygen participation in understanding trends in the oxygen evolution reaction on perovskites. *ACS Catal.* **2018**, *8*, 4628. [[CrossRef](#)]
21. Hong, W.T.; Stoerzinger, K.A.; Lee, Y.L.; Giordano, L.; Grimaud, A.; Johnson, A.M.; Hwang, J.; Crumlin, E.J.; Yang, W.L.; Shao-Horn, Y. Charge-transfer-energy-dependent oxygen evolution reaction mechanisms for perovskite oxides. *Energ. Environ. Sci.* **2017**, *10*, 2190–2200. [[CrossRef](#)]
22. Suntivich, J.; May, K.J.; Gasteiger, H.A.; Goodenough, J.B.; Shao-Horn, Y. A perovskite oxide optimized for oxygen evolution catalysis from molecular orbital principles. *Science* **2011**, *334*, 1383–1385. [[CrossRef](#)] [[PubMed](#)]
23. Han, B.H.; Risch, M.; Lee, Y.L.; Ling, C.; Jia, H.F.; Shao-Horn, Y. Activity and stability trends of perovskite oxides for oxygen evolution catalysis at neutral ph. *Phys. Chem. Chem. Phys.* **2015**, *17*, 22576–22580. [[CrossRef](#)] [[PubMed](#)]
24. Kim, B.; Fabbri, E.; Abbott, D.F.; Cheng, X.; Clark, A.H.; Nachtegaal, M.; Borlaf, M.; Castelli, I.E.; Graule, T.; Schmidt, T.J. Functional role of fe-doping in co-based perovskite oxide cata-lysts for oxygen evolution reaction. *J. Am. Chem. Soc.* **2019**. accepted.
25. May, K.J.; Carlton, C.E.; Stoerzinger, K.A.; Risch, M.; Suntivich, J.; Lee, Y.L.; Grimaud, A.; Shao-Horn, Y. Influence of oxygen evolution during water oxidation on the surface of perovskite oxide catalysts. *J. Phys. Chem. Lett.* **2012**, *3*, 3264–3270. [[CrossRef](#)]
26. Risch, M.; Grimaud, A.; May, K.J.; Stoerzinger, K.A.; Chen, T.J.; Mansour, A.N.; Shao-Horn, Y. Structural changes of cobalt-based perovskites upon water oxidation investigated by exafs. *J. Phys. Chem. C* **2013**, *117*, 8628–8635. [[CrossRef](#)]
27. Fabbri, E.; Nachtegaal, M.; Binninger, T.; Cheng, X.; Kim, B.; Durst, J.; Bozza, F.; Graule, T.; Schaublin, R.; Wiles, L.; et al. Dynamic surface self-reconstruction is the key of highly active perovskite nano-electrocatalysts for water splitting. *Nat. Mater.* **2017**, *16*, 925–932. [[CrossRef](#)] [[PubMed](#)]
28. Suntivich, J.; Gasteiger, H.A.; Yabuuchi, N.; Nakanishi, H.; Goodenough, J.B.; Shao-Horn, Y. Design principles for oxygen-reduction activity on perovskite oxide catalysts for fuel cells and metal-air batteries. *Nat. Chem.* **2011**, *3*, 546–550. [[CrossRef](#)] [[PubMed](#)]

29. Burke, M.S.; Kast, M.G.; Trotochaud, L.; Smith, A.M.; Boettcher, S.W. Cobalt-iron (oxy)hydroxide oxygen evolution electrocatalysts: The role of structure and composition on activity, stability, and mechanism. *J. Am. Chem. Soc.* **2015**, *137*, 3638–3648. [[CrossRef](#)] [[PubMed](#)]
30. Gong, M.; Li, Y.G.; Wang, H.L.; Liang, Y.Y.; Wu, J.Z.; Zhou, J.G.; Wang, J.; Regier, T.; Wei, F.; Dai, H.J. An advanced ni-fe layered double hydroxide electrocatalyst for water oxidation. *J. Am. Chem. Soc.* **2013**, *135*, 8452–8455. [[CrossRef](#)] [[PubMed](#)]
31. Zou, S.H.; Burke, M.S.; Kast, M.G.; Fan, J.; Danilovic, N.; Boettcher, S.W. Fe (oxy)hydroxide oxygen evolution reaction electrocatalysis: Intrinsic activity and the roles of electrical conductivity, substrate, and dissolution. *Chem. Mater.* **2015**, *27*, 8011–8020. [[CrossRef](#)]
32. Trotochaud, L.; Young, S.L.; Ranney, J.K.; Boettcher, S.W. Nickel-iron oxyhydroxide oxygen-evolution electrocatalysts: The role of intentional and incidental iron incorporation. *J. Am. Chem. Soc.* **2014**, *136*, 6744–6753. [[CrossRef](#)] [[PubMed](#)]
33. Dionigi, F.; Strasser, P. Nife-based (oxy)hydroxide catalysts for oxygen evolution reaction in non-acidic electrolytes. *Adv. Energy Mater.* **2016**, *6*, 1600621. [[CrossRef](#)]
34. Chen, J.Y.C.; Dang, L.N.; Liang, H.F.; Bi, W.L.; Gerken, J.B.; Jin, S.; Alp, E.E.; Stahl, S.S. Operando analysis of nife and fe oxyhydroxide electrocatalysts for water oxidation: Detection of fe4+ by mossbauer spectroscopy. *J. Am. Chem. Soc.* **2015**, *137*, 15090–15093. [[CrossRef](#)] [[PubMed](#)]
35. Gorlin, M.; Chernev, P.; de Araujo, J.F.; Reier, T.; Dresp, S.; Paul, B.; Krahnert, R.; Dau, H.; Strasser, P. Oxygen evolution reaction dynamics, faradaic charge efficiency, and the active metal redox states of ni-fe oxide water splitting electrocatalysts. *J. Am. Chem. Soc.* **2016**, *138*, 5603–5614. [[CrossRef](#)] [[PubMed](#)]
36. Gorlin, M.; de Araujo, J.F.; Schmies, H.; Bernsmeier, D.; Dresp, S.; Gliech, M.; Jusys, Z.; Chernev, P.; Krahnert, R.; Dau, H.; et al. Tracking catalyst redox states and reaction dynamics in ni-fe oxyhydroxide oxygen evolution reaction electrocatalysts: The role of catalyst support and electrolyte ph. *J. Am. Chem. Soc.* **2017**, *139*, 2070–2082. [[CrossRef](#)] [[PubMed](#)]
37. Abbott, D.F.; Fabbri, E.; Borlaf, M.; Bozza, F.; Schäublin, R.; Nachttegaal, M.; Graule, T.; Schmidt, T.J. Operando x-ray absorption investigations into the role of fe in the electrochemical stability and oxygen evolution activity of ni1–xfexoy nanoparticles. *J. Mater. Chem. A* **2018**, *6*, 24534–24549. [[CrossRef](#)]
38. Abbott, D.F.; Meier, M.; Meseck, G.R.; Fabbri, E.; Seeger, S.; Schmidt, T.J. Silicone nanofilament-supported mixed nickel-metal oxides for alkaline water electrolysis. *J. Electrochem. Soc.* **2017**, *164*, F203–F208. [[CrossRef](#)]
39. Heel, A.; Vital, A.; Holtappels, P.; Graule, T. Flame spray synthesis and characterisation of stabilised zro2 and ceo2 electrolyte nanopowders for sofc applications at intermediate temperatures. *J. Electroceram.* **2009**, *22*, 40–46. [[CrossRef](#)]
40. Han, B.H.; Grimaud, A.; Giordano, L.; Hong, W.T.; Diaz-Morales, O.; Yueh-Lin, L.; Hwang, J.; Charles, N.; Stoerzinger, K.A.; Yang, W.L.; et al. Iron-based perovskites for catalyzing oxygen evolution reaction. *J. Phys. Chem. C* **2018**, *122*, 8445–8454. [[CrossRef](#)]
41. Binninger, T.; Mohamed, R.; Waltar, K.; Fabbri, E.; Levecque, P.; Kotz, R.; Schmidt, T.J. Thermodynamic explanation of the universal correlation between oxygen evolution activity and corrosion of oxide catalysts. *Sci. Rep.* **2015**, *5*, 12167. [[CrossRef](#)] [[PubMed](#)]
42. Kim, B.J.; Abbott, D.F.; Cheng, X.; Fabbri, E.; Nachttegaal, M.; Bozza, F.; Castelli, I.E.; Lebedev, D.; Schaublin, R.; Coperet, C.; et al. Unraveling thermodynamics, stability, and oxygen evolution activity of strontium ruthenium perovskite oxide. *ACS Catal.* **2017**, *7*, 3245–3256. [[CrossRef](#)]
43. Bick, D.S.; Kindsmuller, A.; Staikov, G.; Gunkel, F.; Muller, D.; Schneller, T.; Waser, R.; Valov, I. Stability and degradation of perovskite electrocatalysts for oxygen evolution reaction. *Electrochim. Acta.* **2016**, *218*, 156–162. [[CrossRef](#)]
44. Battle, P.D.; Gibb, T.C.; Strange, R. A study of a new incommensurate phase in the system srnm1-xcxo3-y. *J. Solid State Chem.* **1989**, *81*, 217–229. [[CrossRef](#)]
45. Gibb, T.C. Evidence for an unusual phase in the perovskite-related system bacoxmn1-xo3-y from exafs spectroscopy. *J. Mater. Chem.* **1992**, *2*, 387–393. [[CrossRef](#)]
46. Gangopadhyay, S.; Inerbaev, T.; Masunov, A.E.; Altilio, D.; Orlovskaya, N. Structural characterization combined with the first principles simulations of barium/strontium cobaltite/ferrite as promising material for solid oxide fuel cells cathodes and high-temperature oxygen permeation membranes. *ACS Appl. Mater. Interfaces* **2009**, *1*, 1512–1519. [[CrossRef](#)] [[PubMed](#)]

47. Ganopadhyay, S.; Masunov, A.E.; Inerbaev, T.; Mesit, J.; Guha, R.K.; Sleiti, A.K.; Kapat, J.S. Understanding oxygen vacancy migration and clustering in barium strontium cobalt iron oxide. *Solid State Ionics* **2010**, *181*, 1067–1073. [CrossRef]
48. Mueller, D.N.; De Souza, R.A.; Brendt, J.; Samuelis, D.; Martin, M. Oxidation states of the transition metal cations in the highly nonstoichiometric perovskite-type oxide $\text{Ba}_{0.1}\text{Sr}_{0.9}\text{Co}_{0.8}\text{Fe}_{0.2}\text{O}_{3-\delta}$. *J. Mater. Chem.* **2009**, *19*, 1960–1963. [CrossRef]
49. Arnold, M.; Xu, Q.; Tichelaar, F.D.; Feldhoff, A. Local charge disproportion in a high-performance perovskite. *Chem. Mater.* **2009**, *21*, 635–640. [CrossRef]
50. Jun, A.; Kim, J.; Shin, J.; Kim, G. Perovskite as a cathode material: A review of its role in solid-oxide fuel cell technology. *ChemElectroChem* **2016**, *3*, 511–530. [CrossRef]
51. Kuklja, M.M.; Kotomin, E.A.; Merkle, R.; Matrikov, Y.A.; Maier, J. Combined theoretical and experimental analysis of processes determining cathode performance in solid oxide fuel cells. *Phys. Chem. Chem. Phys.* **2013**, *15*, 5443–5471. [CrossRef] [PubMed]
52. Glazer, A.M. Simple ways of determining perovskite structures. *Acta Cryst. Sect. A* **1975**, *31*, 756–762. [CrossRef]
53. Risch, M. Perovskite electrocatalysts for the oxygen reduction reaction in alkaline media. *Catalysts* **2017**, *7*, 154. [CrossRef]
54. Heel, A.; Holtappels, P.; Hug, P.; Graule, T. Flame spray synthesis of nanoscale $\text{La}_{0.65}\text{Sr}_{0.4}\text{Co}_{0.2}\text{Fe}_{0.8}\text{O}_{3-\delta}$ and $\text{Ba}_{0.5}\text{Sr}_{0.5}\text{Co}_{0.8}\text{Fe}_{0.2}\text{O}_{3-\delta}$ as cathode materials for intermediate temperature solid oxide fuel cells. *Fuel Cells* **2010**, *10*, 419–432. [CrossRef]
55. Muller, O.; Nachtegaal, M.; Just, J.; Lutzenkirchen-Hecht, D.; Frahm, R. Quick-exafs setup at the superxas beamline for in situ x-ray absorption spectroscopy with 10 ms time resolution. *J. Synchrotron Radiat.* **2016**, *23*, 260–266. [CrossRef] [PubMed]
56. Ravel, B.; Newville, M. Athena, artemis, hephaestus: Data analysis for x-ray absorption spectroscopy using ifeffit. *J. Synchrotron Radiat.* **2005**, *12*, 537–541. [CrossRef] [PubMed]
57. Delaplane, R.G.; Ibers, J.A.; Ferraro, J.R.; Rush, J.J. Diffraction and spectroscopic studies of cobaltic acid system $\text{HCOO}_2\text{-DCOO}_2$. *J. Chem. Phys.* **1969**, *50*, 1920–1927. [CrossRef]
58. Schmidt, T.J.; Gasteiger, H.A.; Stab, G.D.; Urban, P.M.; Kolb, D.M.; Behm, R.J. Characterization of high-surface area electrocatalysts using a rotating disk electrode configuration. *J. Electrochem. Soc.* **1998**, *145*, 2354–2358. [CrossRef]
59. Binninger, T.; Fabbri, E.; Patru, A.; Garganourakis, M.; Han, J.; Abbott, D.F.; Sereda, O.; Kotz, R.; Menzel, A.; Nachtegaal, M.; et al. Electrochemical flow-cell setup for in situ x-ray investigations i. Cell for saxs and xas at synchrotron facilities. *J. Electrochem. Soc.* **2016**, *163*, H906–H912. [CrossRef]
60. Castelli, I.E.; Huser, F.; Pandey, M.; Li, H.; Thygesen, K.S.; Seger, B.; Jain, A.; Persson, K.A.; Ceder, G.; Jacobsen, K.W. New light-harvesting materials using accurate and efficient bandgap calculations. *Adv. Energy Mater.* **2015**, *5*, 1400915. [CrossRef]
61. The Materials Project. Available online: <https://materialsproject.org/> (accessed on 17 November 2017).
62. Johnson, J.W.; Oelkers, E.H.; Helgeson, H.C. Supcrt92 - a software package for calculating the standard molal thermodynamic properties of minerals, gases, aqueous species, and reactions from 1-bar to 5000-bar and 0-degrees-c to 1000-degrees-c. *Comput. Geosci.* **1992**, *18*, 899–947. [CrossRef]
63. Pourbaix, M. Atlas of Electrochemical Equilibria in Aqueous Solutions. Pergamon Press: Oxford, UK, 1966.
64. Larsen, A.H.; Mortensen, J.J.; Blomqvist, J.; Castelli, I.E.; Christensen, R.; Dulak, M.; Friis, J.; Groves, M.N.; Hammer, B.; Hargus, C.; et al. The atomic simulation environment-a python library for working with atoms. *J. Phys. Condens. Mat.* **2017**, *29*, 273002.
65. Persson, K.A.; Waldrick, B.; Lazic, P.; Ceder, G. Prediction of solid-aqueous equilibria: Scheme to combine first-principles calculations of solids with experimental aqueous states. *Phys. Rev. B* **2012**, *85*. [CrossRef]
66. Castelli, I.E.; Thygesen, K.S.; Jacobsen, K.W. Calculated optical absorption of different perovskite phases. *J. Mater. Chem. A* **2015**, *3*, 12343–12349. [CrossRef]
67. Giannozzi, P.; Baroni, S.; Bonini, N.; Calandra, M.; Car, R.; Cavazzoni, C.; Ceresoli, D.; Chiarotti, G.L.; Cococcioni, M.; Dabo, I.; et al. Quantum espresso: A modular and open-source software project for quantum simulations of materials. *J. Phys. Condens. Mat.* **2009**, *21*, 395502. [CrossRef] [PubMed]

68. Perdew, J.P.; Ruzsinszky, A.; Csonka, G.I.; Vydrov, O.A.; Scuseria, G.E.; Constantin, L.A.; Zhou, X.L.; Burke, K. Restoring the density-gradient expansion for exchange in solids and surfaces. *Phys. Rev. Lett.* **2008**, *100*. [[CrossRef](#)] [[PubMed](#)]
69. Standard Solid State Pseudopotential Library. Available online: <http://materialscloud.org/sssp> (accessed on 17 November 2017).



© 2019 by the authors. Licensee MDPI, Basel, Switzerland. This article is an open access article distributed under the terms and conditions of the Creative Commons Attribution (CC BY) license (<http://creativecommons.org/licenses/by/4.0/>).